We are IntechOpen,
the world's leading publisher of
Open Access books
Built by scientists, for scientists

6,900
Open access books available

186,000
International authors and editors

200M
Downloads

Our authors are among the

154
Countries delivered to

TOP 1%
most cited scientists

12.2%
Contributors from top 500 universities

BOOK CITATION INDEX
CLARIVATE ANALYTICS
INDEXED

WEB OF SCIENCE™

Selection of our books indexed in the Book Citation Index
in Web of Science™ Core Collection (BKCI)

Interested in publishing with us?
Contact book.department@intechopen.com

Numbers displayed above are based on latest data collected.
For more information visit www.intechopen.com

Nonlinear Microscopy Techniques: Principles and Biomedical Applications

Javier Adur, Hernandes F. Carvalho,
Carlos L. Cesar and Víctor H. Casco

Additional information is available at the end of the chapter

Abstract

Nonlinear optical microscopy techniques have emerged as a set of successful tools within the biomedical research field. These techniques have been successfully used to study autofluorescence signals in living tissues, structural protein arrays, and to reveal the presence of lipid bodies inside the tissular volume. In the first section, the nonlinear contrast technique foundations is described, and also, a practical approach about how to build and combine this setup on a single confocal system platform shall be provided. In the next section, examples of the usefulness of these approaches to detect early changes associated with the progression of different epithelial and connective tissular diseases are presented.

Finally, in the last section, we attempt to review the present-day most relevant analysis methods used to improve the accuracy of multimodal nonlinear images in the detection of epithelial cancer and the supporting stroma. These methods are presented as a set of potential valuable diagnostic tools for early cancer detection and to differentiate clinical subtypes of *osteogenesis imperfecta* disorders, being highly advantageous over present classical clinical diagnostic procedures.

In this chapter, it is proposed that the combination of nonlinear optical microscopy and informatics-based image analysis approaches may represent a powerful tool to investigate collagen organization in skin diseases and tumor cell morphology.

Keywords: nonlinear microscopy, second harmonic generation, third harmonic generation, image analysis, early diagnosis

INTECH
open science | open minds

1. Principles of nonlinear microscopy techniques

The notable advances in cell and molecular biology science have induced the need to imagine cells in an intact-live whole organism. Therefore, the need for real-time observation of cell (and their subcellular components) behavior in whole tissues has become crucial to understanding cellular physiology. During the past decades, imaging techniques have been improved to pursue this goal. One of these techniques is fluorescence imaging. The use of confocal microscopy allows the examination of subcellular material with three-dimensional resolution but is restricted by the effective imaging depth (usually less than 200 μm) and phototoxicity, which is caused by using a short wavelength laser (principally continuous wave (CW) laser) [1]. Recent advances in nonlinear optical processes of multiphoton microscopy overcome single-photon linear microscopy technologies, such as confocal microscopy, by their capacity of tissular penetration, clean images production, minimal invasiveness, and chemical selectivity [2]. Therefore, multiphoton fluorescence (MPF) and nonlinear optical (NLO) microscopy in recent year has become one of the key imaging modes and evolved as an alternative to conventional single-photon confocal microscopy. The best-known nonlinear microscopy techniques are two-photon excited fluorescence (TPEF) microscopy, second harmonic generation (SHG) and third harmonic generation (THG) microscopy, and coherent anti-Stokes Raman scattering (CARS) microscopy.

These nonlinear technologies provide several advantages, namely high depth penetration by using a near infrared (pulsed) laser as excitation source, intrinsic tridimensional sectioning and resolution, due to the spatial confinement of the signal to the laser focus, multiple nonlinear processes, and the possibility to use numerous endogenous molecular markers and low phototoxicity that allows the investigation of living processes, without significant perturbation [3]. Together, these advantages allow analyzing the complex relations between tissue and organ function and its structure in complex diseases [4].

To understand this new microscopy instruments, it is advisable to think in classical optical tool. In conventional optical imaging, contrast mechanisms consist of interactions such as absorption, reflection, scattering, and fluorescence, and the response recorded is linearly dependent on the intensity of the incident light. Thereby, there is a linear relationship between the strength of electric field of the light and the induced object polarization. At moderately low incident intensity, the optical response can be approximated to the first-order response as $P = \chi^{(1)} \otimes E$, where $\chi^{(1)}$ is the linear susceptibility, P is the polarization of a material, and E is the strength of an applied optical field. By contrast, nonlinear optical effects occur when a biological tissue interacts with an intense laser beam exhibiting a nonlinear response to the applied field strength. In this situation, the induced polarization vector P of the material subject to the vectorial electric field E can be expressed as $P = \chi^{(1)} \otimes E + \chi^{(2)} \otimes E \otimes E + \chi^{(3)} \otimes E \otimes E \otimes E$ +…, where $\chi^{(i)}$ is the $i^{\text{(th)}}$ order nonlinear susceptibility tensor and $\otimes$ represents a combined tensor product and integral over frequencies [5]. The bulk nonlinear optical susceptibilities $\chi^{(2)}$ and $\chi^{(3)}$ are obtained from the corresponding high-order molecular nonlinear optical coefficients (hyperpolarizability) β and γ by using a sum of the molecular coefficients over all molecule sites. Typically, materials with conjugated π-electron structures exhibit large optical

nonlinearities. The usual linear susceptibility $\chi^{(1)}$ contributes to the single-photon absorption and reflection of the light in tissues. The $\chi^{(3)}$ corresponds to third-order processes such as two-photon absorption, THG, and CARS, while SHG results from $\chi^{(2)}$ [6].

Another way is to think nonlinear optical processes in terms of particles called photons discovered by Einstein, such as processes involving more than one photon. All these processes have some characteristics in common. First, it only occurs if multiple photons coincide in time and space or, in chemical terms, at high concentration of photons. The speed V of a chemical reaction of n elements $f + f + f + f +\ldots \rightarrow f_n$ depends on the concentration f elevated to the nth degree, that is, $V \propto [f]^n$ where $[f]$ is the concentration of f. In optics, the concentration is proportional to the laser beam intensity, I = power/area = (energy/time) / area. Thus, the efficiency of a one-photon process is I, and for two-photon would be I^2, and generalizing for n photons I^n. Therefore, it is not surprising that the first nonlinear optical empirical results were materialized only after the advent of pulsed lasers. The NLO microscopes come with the advent of Ti:Sa lasers which produce pulses typically in the range of 100 femtoseconds [fs = 10^{-15} sec], with an average power of 2 watts and repetition time of 12 nanoseconds [ns = 10^{-9} sec]. In this case, the peak power will be 240 kilowatts, although the pulse energy is just 24 nanoJoule. The pulsed laser, therefore, increased the peak power of 2 watts for a CW laser to 240 kilowatts, while keeping the same average power and low energy per pulse. In other words, the very high potencies are obtained by decreasing the pulse duration instead of increasing the pulse energy. Thus, nonlinear effects occur avoiding the potential sample damage. The smaller the temporal pulse duration, greater the efficiency of nonlinear processes, so femtosecond lasers are preferable to picosecond lasers.

The pulsed laser ensures the coincidence of photons in time, but not in the space. The concentration of photons but will be greater the smaller the area of the laser beam, i.e., is maximum in the laser focus. The total generation of events caused by one photon processes is constant, independent of the laser focusing position, because if the process is linear with I, the total number of events is proportional to I multiplied by the area, i.e., N events $\propto$ (power/area) × area = power. As power is constant along the beam, the number of events does not depend on the axial position [along the lens axis—defined as the z-axis]. The processes with more than one photon are proportional to I^n and therefore are inherently confocal. In this case, the amount of events depends very strongly on the beam area, because now N events $\propto I^n$ × area = (power^n/area^{n-1}). Two-photon processes decay inversely with the area, whereas a three-photon does so with the square of the area. This means that events can occur only in the vicinity of the lower area, i.e., the laser focus, that is, the light generated by the nonlinear optical process are generated at the focus of the laser, which becomes intrinsically a confocal microscope. The laser focus is on the operator microscope control and can be used for 3D image reconstruction.

One way to visualize the various nonlinear optical processes is by arrows with length proportional to the photon energy. **Figure 1** schematically depicts a number of nonlinear optical effects, produced for the specimen if the energy density at the focal spot of an objective lens is sufficiently large and also are compared with lineal process produced for a CW laser. Principal contrast mechanisms and characteristics of TPEF, SHG, THG, and CARS modalities are described below.
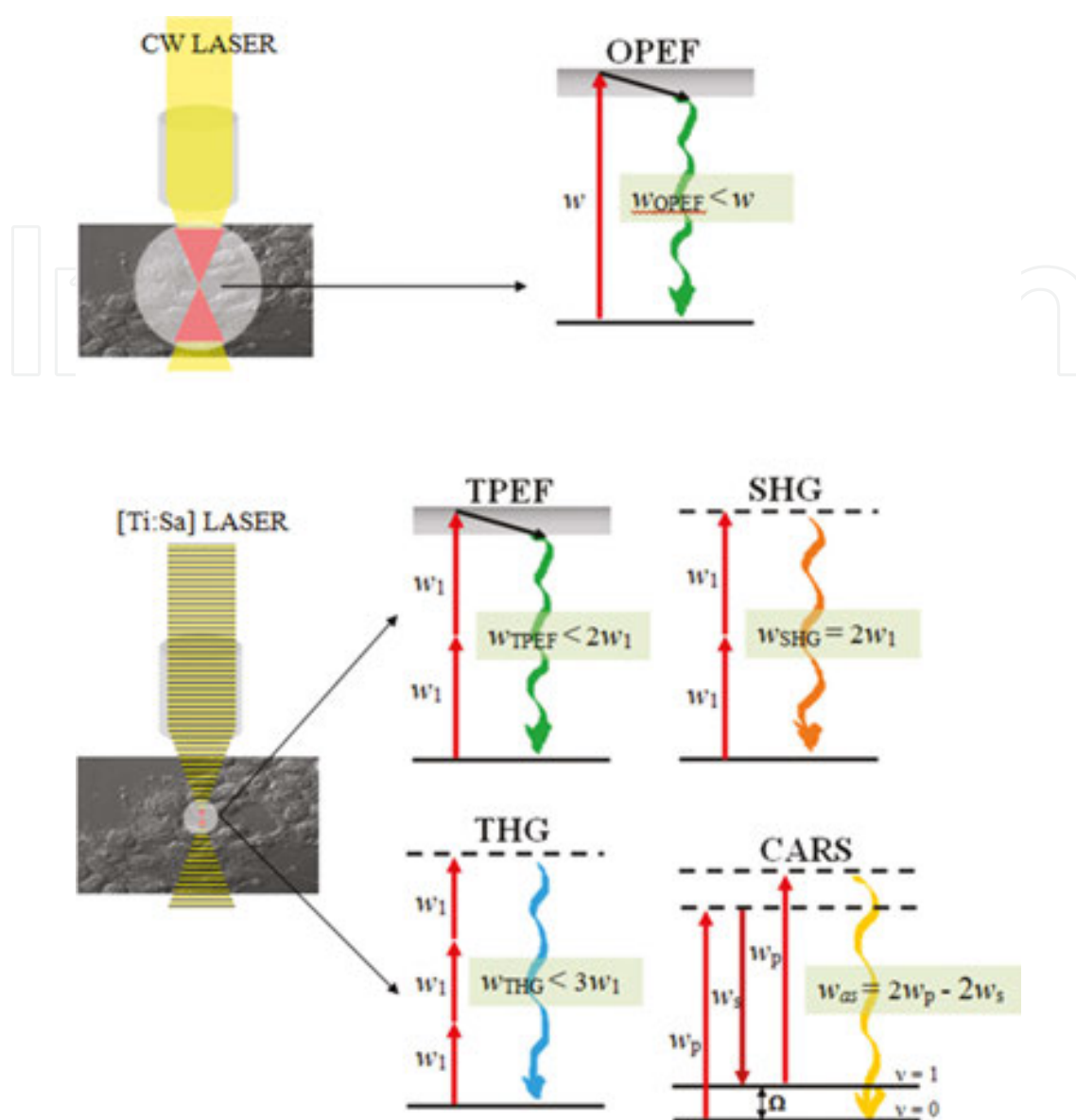
Figure 1. Energy diagrams of linear and nonlinear optical process. Solid lines represent electronic and vibrational states of molecules, while dashed lines denote virtual states. The straight arrows are excitation beams, whereas wavy arrows are the output signal beams. The black arrow represents relaxation in electronically excited states, and red hourglass represents the excitation volume. $\omega 1$ and $\omega 2$ symbolize the two beams available in CARS microscope. $\omega p = \omega 1$ and $\omega s = \omega 2$ in CARS. $v = 0$: vibrational ground state, $v = 1$: vibrational excited state, and Ω is a frequency of vibrational transition between $v = 0$ and $v = 1$. $\omega 1$ = pump beams and $\omega 2$ = Stokes beam from the laser sources. $\omega 3$ is a long wavelength beam for THG obtainable on OPO systems for CARS microscope. Abbreviations: CW: continuous wave, OPEF: one-photon excited fluorescence, OPO: optical parametric oscillator.

TPEF microscopy is a third-order nonlinear optical resonant process where two photons excite an electron from the ground state. It is an inelastic process where photon energy is released at the sample. Two-photon absorption happens only when the energy of the incident photons falls into the two-photon excitation band which is specific for each fluorescent marker. The two-photon excitation band is not exactly half of the one photon excitation band because the selection rules are different. The fact that TPE depends on the square of the incident light

provides its confocal features, that is, a process happening only at a focal point volume. Photobleaching is smaller in two-photon excited fluorescence (TPEF) compared to single photon excitation because the excited volume is smaller. Multicolor imaging is allowed to excite different fluorophores simultaneously through different order processes with a single wavelength, in which emissions are spectrally shifted by hundreds of nanometers and uninterrupted for collection. Consequently, multiphoton microscopy is especially appropriate for physiological and pathophysiological studies since it is able to excite endogenous auto-fluorescent components and thus to obtain specific signals such as nicotinamide adenine dinucleotide (NADH) and flavin adenine dinucleotide (FAD) [6].

On the contrary, SHG and THG are coherent second/third-order elastic nonlinear optical processes, respectively. Because two/three photons generate another photon with two/three times the energy of the incident photons, there is no energy released to the medium, meaning out of focus cell photodamages are not expected from these processes. Both SHG/THG can be segregated from fluorescence signals by the wavelength or even by time gating, because the coherent processes are practically instantaneous. The fact that SHG signal is proportional to I^2, while THG signal is proportional to I^3, where I, is the incident light intensity, provides confocality for both techniques. For the same wavelength of the incident light, THG has better optical sectioning resolution than SHG or TPEF but is also more sensitive to changes in the intensity of the light in the focused spot, such as those caused by laser instability or by scattering or defocusing the illumination [7]. The first images of high-resolution SHG were reported in 1998 by Sheppard's group [8], and shortly afterward in 2001, Chu and co-workers showed a multimodal imaging study, including TPEF+SHG+THG [9]. Usually, the third-order nonlinear susceptibility (χ^3), responsible for THG, is much smaller than the second-order one (χ^2), responsible for SHG. In principle, this would mean that THG should be much harder to observe. However, χ^2, as well as any other even susceptibility coefficients, must be null in the presence of inversion symmetry. Therefore, SHG shall be zero in the presence of centro-symmetric molecules, unless an external parameter, such as electric fields or interfaces, breaks the symmetry.

By contrast, all materials have non-zero third-order susceptibility χ^3. Moreover, $\chi3$ can be several orders of magnitude larger or smaller for different materials. However, THG is null in a homogeneous material, no matter how high χ^3 could be, because the Gouy-phase shift of π across the focus of a Gaussian excitation beam creates a destructive interference between signals generated before and after the focus [10]. Nevertheless, for a nonhomogeneous focal volume, a measurable amount of third harmonic is generated [11]. Since in biological samples, heterogeneity is more common than homogeneity, THG provides an important tool for bioimaging, with the warning that it tends to be brighter at the interface of large granules, lipid droplets, or similar biostructures, compared to the internal signal [6]. SHG imaging modality can probe molecular organization, molecular symmetry, orientation, molecular alignments, and ultrastructure on the micro, as well as the nanoscale. Natural structures are mostly unarranged (optically isotropic) and do not generate any SHG signal. Hardly, some few biological assemblies are ordered and can produce harmonic signal. One of the best known SHG structures in biology is collagen, the major protein of the extracellular matrix. Collagen

fibrils often aggregate into larger, cable-like bundles, several micrometers in diameter. This regularly staggered packing order provides the needed structural conditions for efficient SHG [12]. Other examples are acto-myosin assemblies in muscle and microtubule structures in living cells [13, 14]. Discontinuities in refraction index of the optical dispersion properties of biological tissues are able to generate THG signals [15, 16]. The THG can be used to study optical cell interfaces such as those at cell membranes or organelle surfaces. For example, the surface of the erythrocyte can generate significant THG [17]. In contrast to the chemical specificity that characterizes fluorescence images, harmonic generation (SHG and THG) provides an imaging modality specific for structural configuration. In the study of cancer tumors, our experience with both techniques is that SHG is an excellent tool to observe collagen network of extracellular matrix, while THG allows to clearly display the nuclei, which are two key parameters for pathologists [4, 18–20].

Characteristics	TPEF	SHG	THG	CARS
Application in bioscience	1990	1986	1997	1982
Number of photons	2	2	3	3
Susceptibility	χ^3	χ^2	χ^3	χ^3
Advantages	Deeper imaging with less phototoxicity Spatial localization forfluorescence excitation	Coherent process, symmetry selection Probing well-ordered structures, functions of membranes, nonfluorescence tissues No absorption of light	Coherent process, no symmetry requirement No absorption of light Imaging both in bulk and at surfaces for extended conjugation of pi electrons	Coherent process Inherent vibrational contrast for the cellular species, requires no endogenous or exogenous fluorophores Vibrational and chemical sensitivities
Contrast mechanics	Electronics levels of the molecules	Nonlinear properties of the medium	Nonlinear properties of the medium	Vibrational levels of the molecules
Information	Autofluorescence of some biological substances (NADH, FAD, etc.)	Noncentrosymmetric molecules with spatial organization (collagen, elastin, etc.)	Interfaces, optical inhomogeneities, (cell edges, lipids, membranes)	Chemical information (lipids, DNA, proteins)

Table 1. Characteristics of nonlinear optical microscopy.

In addition to harmonic generation microscopy, CARS microscopy is another 3D high-resolution imaging approach that circumvents exogenous probes. CARS is a four-wave mixing

process in which a pump beam at frequency w_p, a Stokes beam at frequency w_s, and a probe beam at frequency w'_p are interacted with a sample to result in an anti-Stokes signal at $w_{as} = 2w_p - w_s$. In nearly all experiments, the pump and the probe beams are derived from the resonant oscillation when the beat frequency $(w_p - w_s)$ matches the frequency of a particular Raman active molecular vibration mode. Furthermore, due to its coherent nature, CARS signal production only occurs when the field-sample interaction length is less than the coherence length. The generated CARS signal is proportional to $(\chi^{(3)})^2 \, I^2_p \, I_s$, having a quadratic dependence on the pump field intensity and a linear dependence on the Stokes field intensity. These properties provide it a 3D-sectioning capability [6]. First CARS microscopy setup was described at the nineties [21] and has now matured into a powerful method for biological imaging. CARS microscopy is more informative than SHG and THG microscopy since it contains rich spectroscopic information about specific molecular species.

To summarize the first section, a description of the physical properties, characteristics, and principal contrast mechanisms of each nonlinear optical imaging method described are summarized in **Table 1**.

2. Nonlinear optical technique implementation

Today, there are multiples ways to assemble a nonlinear microscopy platform. The engineering challenge is to integrate the different modalities on a single platform. In response to this challenge, manufacturers have designed microscopes with multiple input and output ports and increased infinity space for the introduction of customized optics. Coming up next, some laser sources, detectors, and confocal body microscopies routinely used in this technology are enumerated, and a setup configuration by our group is described in some detail.

As was described in the introductory section, for high harmonic generation and multiphoton fluorescence microscopies, short femtoseconds pulses of high peak power are required. While ultrashort few cycle pulses are spectrally very broad, they allow for simultaneous excitation of different chromospheres with spectrally separated absorption bands. Available lasers that conjugate these features are the titanium:sapphire (Ti:Sa) (wavelength range 700–980 nm, pulse width 100 fs, and 76–100 MHz repetition rate), the Cr:forsterite laser (wavelength range 1230–1270 nm, pulse width 65 fs, and 76–120 MHz repetition rate), the Nd:glass laser (wavelength range 1053–1064 nm, pulse width 150 fs, and 70–150 MHz repetition rate), and the femtosecond ytterbium laser (wavelength range 1030 nm, pulse width 200 fs, and 50 MHz repetition rate).

The SHG wavelength excited by a Ti:Sa femtosecond laser operating at 940 nm will be in the blue at 470 nm, and the TPEF will be in the region above 470 nm. While that THG signal generated by a 940 nm principal beam, will be in the UV region at 330 nm. As a result, the THG signal will suffer from the high UV absorption of the principal biological specimens making signal detection difficult. In contrast, using the Cr:forsterite laser operating in the range of 1230 nm allows SHG (615 nm), THG (410 nm), and TPEF (>615 nm), all to fall within the visible spectrum. Additionally, the lowest light attenuation in biological material is generally found in the 1000–1300 nm. In recent years other ultrafast laser systems appeared, such as InSight TM DeepSee TM (wavelength range 680–1300 nm, pulse width <120 fs, and repetition rate 80

MHz), which also can be an excellent light source for multi-modality microscopy. Moving the excitation wavelength to 1200 nm, not only the visible but also the NIR spectrum is open for signal recording.

Nonlinear microscopes share many common features with confocal laser scanning microscopes. In fact, many research groups have implemented multimodal nonlinear platform by coupling source lasers described previously into a confocal scanning microscope. Practically, many scan head models of different manufactures have been used with this proposal, such as Olympus FV300 [22], Olympus FV1000 [23], Zeiss LSM Meta 510 [24], Zeiss LSM 710 [25], Nikon C1 [26], Leica TCS-SP5 [27], and Zeiss LSM 780 [28]. In general, the generated nonlinear signals can be collected with the same microscope objective, separated by a dichroic mirror, which is expressly selected for the given fundamental and fluorescence or harmonic emission wavelengths and focused with a lens through the filter onto detector. If Ti:Sa laser is used, the wavelengths fall within the sensitivity range of high quantum efficiency (QE) silicon-based detectors and photomultiplier tube (PMT) photocathodes that are the currently used detectors. If the source laser used are Nd:glass or Cr:forsterite, special NIR detectors (i.e., indium gallium arsenide (InGaAs) photodiode) are needed. For more data about the optical characteristics of the different detectors, readers can find excellent information in [7].

In our setup (**Figure 2**), we used an inverted Zeiss Axio Observer.Z1 and confocal LSM 780. Briefly, this device is equipped with a UV-lamp, for classical epi-fluorescence operation mode; five lines of CW laser, for confocal studies; and femtosecond (fs) and picosecond (ps) pulsed laser, for nonlinear microscope modalities. The fs laser source is a tunable, Ti:sapphire laser emitting around 690–1040 nm both for efficient TPEF and higher SHG/THG spatial resolution. The picosecond (ps) source is obtained from a synchronously pumped optical parametric oscillator (OPO) system to obtain THG signal in the visible range and high spectral resolution CARS microscopy. The OPO can be easily and continuously tuned over a wide spectral range from 690 to 990 nm for the signal and between 1150 and 2450 nm for the idler output. The fs laser is combined with the scan head through an acousto-optic modulator (AOM) and a collimating telescope (T1) to regulate the beam diameter in the objective back-aperture and the focus position on the microscope focal point. The five wavelengths (signal and idler for each OPO plus the fundamental 1064 nm) are controlled independently with dedicated telescopes (T2, T3, T4, T5, and T6). Delay lines on the five beam paths ensure temporal overlap between the beams. These beams necessary for CARS microscopy are temporally synchronized, recombined (P), and sent onto the backward excitation port of the scan head. The scan head of the LSM780 has a spectral gallium arsenide phosphide (GaAsP) detector with 32 in-line elements and 2 adjacent PMTs. The motorized collimators, the scanners, and the pinhole precisely positionable and the highly sensitive detectors are arranged to provide optimum specimen illumination and efficient collection of the emitted light. The Raman line width is comparable to the spectral width of a picosecond pulse, so that the excitation energy is fully used to take full advantage of the vibrational resonant CARS signal. Working with 1~3 ps spectral pulse widths is possible to obtain the optimal signal-to-background ratio for typical Raman band [29]. A pulse width of a few picoseconds provides a good compromise between the spectral resolution and the peak power and improves the signal-to-background ratio. The
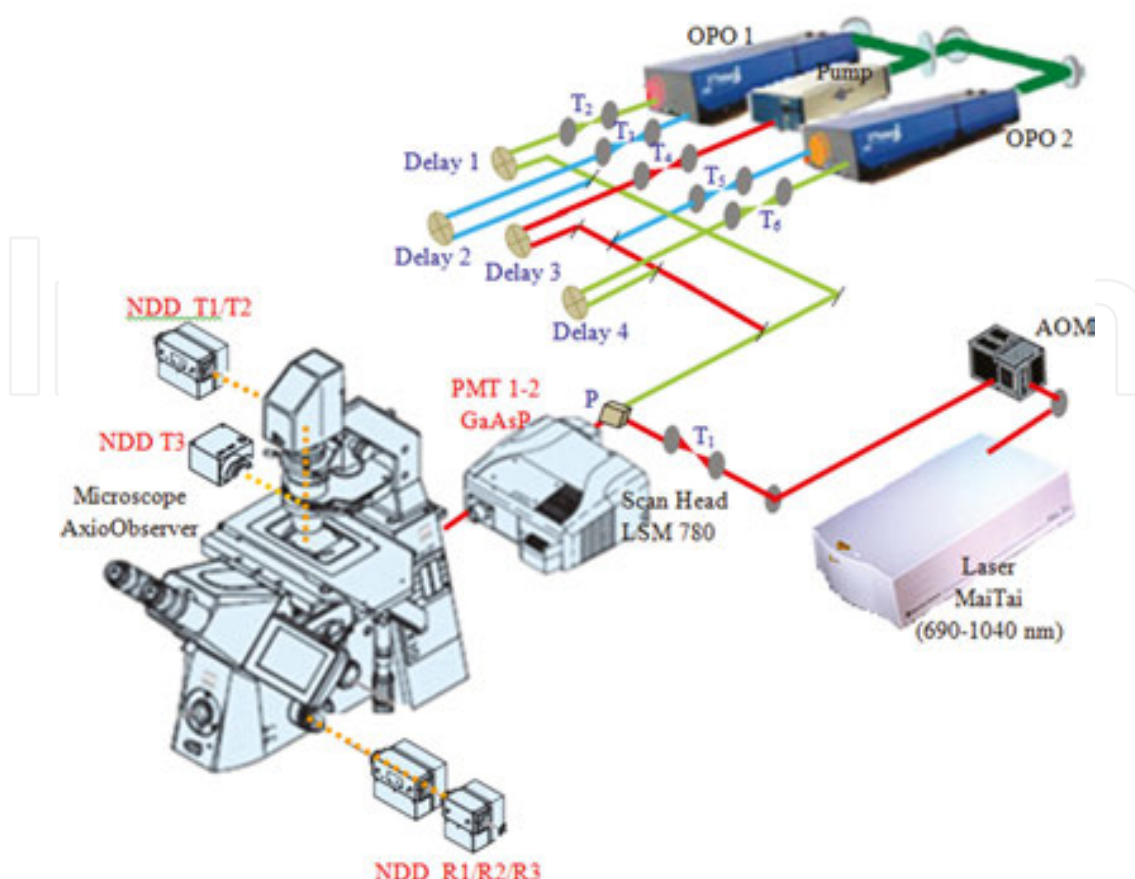
Figure 2. Schematic setup of a multimodal NLO microscope using a femtosecond laser source (Mai-Tai) and picoseconds (OPOs system) pulsed laser. Lasers are coupled to a commercial confocal system platform (inverted Zeiss Axio Observer.Z1 and confocal LSM 780). Principal optics elements are shown with blue letterings (telescope, delay lines, and recombination) and detectors with red letterings. Solid and dashed lines represent excitation and emission paths, respectively. AOM, acousto-optic modulator; T, telescope lens; P, recombine; NDD T, nondescanned detector (transmitted way); NDD R, nondescanned detector (reflective way); PMT, photomultiplier tube.

OPO light source for CARS that we used has already been reported to perform time resolved CARS [30] to improve the sensitivity or to cover the full vibrational Raman spectrum. In our setup, the frequency doubled Nd:YVO generates 8 W of green light (532 nm) and pumps two OPOs with 4 W each. Although the full system can provide up to five wavelengths simultaneously (signal and idler for each OPO plus the fundamental 1064 nm), we normally use three colors. The two signals coming from each OPO are recombined with the fundamental 1064 nm beam from the Nd:YVO oscillator. The power, polarization state, and divergence of each beam are controlled independently with dedicated polarization optics and telescopes. Delay lines on two of the beam paths (signal and 1064 nm) assure temporal overlap between the three beams. The backward detection is achieved with internal GaAsP detector of scan head. A set of dedicated filters is placed before the detectors to select the relevant spectral domains.

The generated signals can be collected with the same microscope objective (reflected or epi-detected), splitted by dichroic mirrors, which were specifically chosen for the given funda-

mental and fluorescence or harmonic emission wavelengths and focused onto specific detectors. Interference or band pass filters are used in front of the detector for filtering scattered fundamental light and spurious signals outside the desired bandwidth. For epidetection, the system has two internal PMT plus GaAsP avalanche photodiodes inside the scan head (PMT 1-2, **Figure 2**). Also, three non-descanned detectors (NDDs) are available for epi-detection of nonlinear signals (NDD R1/R2/R3). It is also possible to detect the signals in the forward direction. Either one detector with appropriate filters or several detectors recording different signals separated by dichroic mirrors can be used. The system shown here has three NDD detectors (NDD T1/T2/T3). T3 detector was placed right after the sample, holding it as close to the sample as possible. With this system, many configurations can be used and different, linear, and/or nonlinear signals can be simultaneously detected. For example, we can observe CARS signal with internal GaAsP detector of scan head, forward THG, SHG and TPEF with NDD T1/T2/T3, and reflected SHG and TPEF with NDD R1/R2.

## 3. Biomedical applications

Over the past years, life science interdisciplinary research has routinely used nonlinear microscopy techniques. The combination of SHG, THG, and CARS is used in the production of chemical maps of complex tissues. NLO techniques allow inspecting the assembly of single cells, tissues, and organs as well as monitoring structural and chemical changes related to diverse diseases. Here a few examples of the use of our setup in two applications are shown, epithelial cancer detection and diagnosis of *osteogenesis imperfecta*.

3.1. Cancer detection

Cancer is still a threat to human life [31]. Modern clinically used imaging methods for cancer diagnosis comprise x-ray, CT, MRI, and OCT [32, 33]. The facilities of these technologies are restricted by either low spatial resolution or a lack of chemical specificity, making it difficult to identify the edges of the tumor. Today, new image-based instruments are necessary as diagnostic tool to evaluate structural features with subcellular resolution that are closely linked with tumor malignancy. The combination of different image approaches described in this chapter may represent a powerful combination of tools to study both malignant cells and stromal environment. One of the main examples of such an objective is the collagen organization changes analysis, the remodeling matrix and alterations in epithelial/stromal interface. Highly valuable, structural information revealed by each nonlinear contrast approach can be isolated and analyzed separately, while their superposition allows a better comparison and understanding of the spatial tissue organization. Thus, TPEF and THG can be used to image a variety of well-documented morphologic and architectural alterations, moreover, combined TPEF-SHG can be applied to analyze alterations in epithelial cells and the supporting stroma, and CARS microscopy can be used to understand lipid and proteins composition in tumor tissues.

Figure 3A exemplifies this combination, where NLO techniques were applied to differentiate between normal and malignant (fibroadenoma and invasive lobular carcinoma (ILC)) human breast tissue. The characteristic microscopic appearance of each type of tissue and relationship between cells and stromal compartment can be identified in the SHG/THG combination. The differential orientation and distribution of collagen fibers can be clearly identified in stromal region with SHG image. **Figure 3B** shows a comparative analysis of CARS images of breast tissue. Adipose and fibrous structures of normal tissue possess strong CARS signals. Fibroadenoma exhibits the compressed duct with linear branching pattern, whereas ILC presents single or rows of cells invading into the stroma. Based on examples such as this and our previous work [19], we have established that it is possible to have both qualitative parameters of differences between each kind of breast tumor and to demonstrate the advantage of the integration of as many NLO approaches as possible to analyze breast cancer.
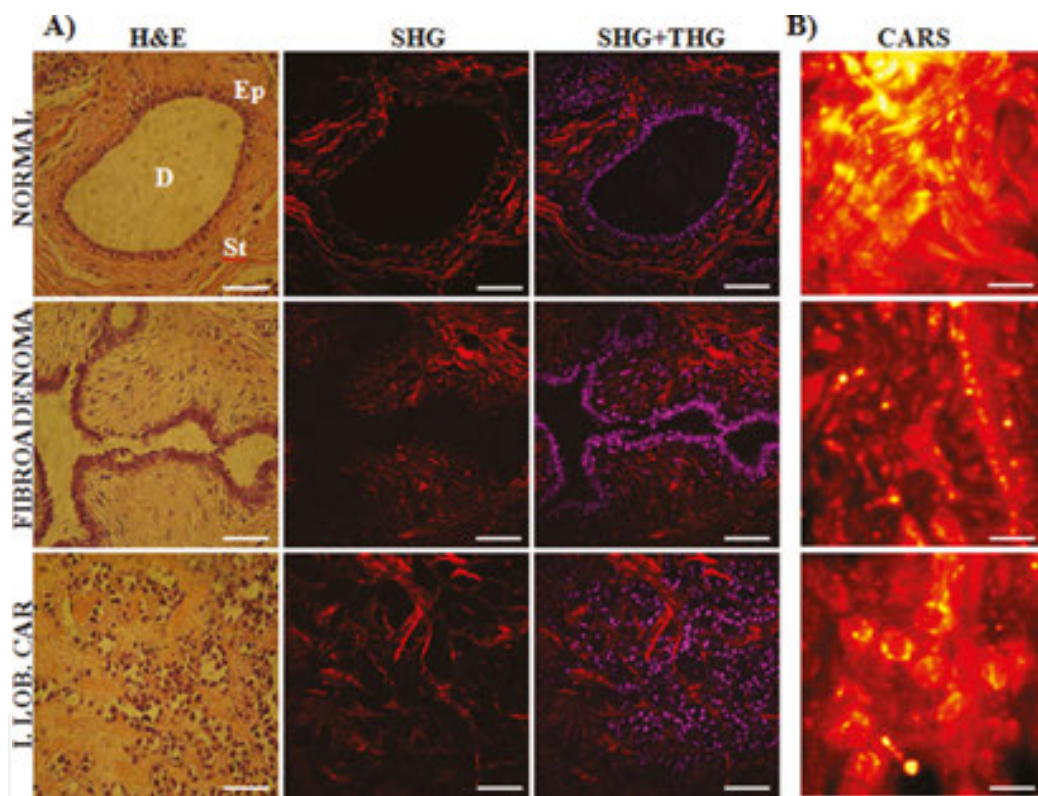
Figure 3. Multimodal NLO approach applied to human breast tumor. (A) Representative H&E-stained and SHG, and SHG+THG cross-sectional images of breast tissues diagnosed as normal (first row), fibroadenoma (second row), and invasive lobular carcinoma (third row). Scale bar = 20 μm. (B) Representative CARS cross-sectional images of breast tissues. Scale bar = 20 μm. D, duct; Ep, epithelium; St, stroma; Fibroad, fibroadenoma; Lob. Carc., lobular carcinoma; I.Lob.Carc, invasive lobular carcinoma. **Figure 3A** from Adur et al., [19].

Human ovarian tumors are shown in **Figure 4**. TPEF signal (green) represents stromal connective tissues. The SHG signal (red) shows collagen fibers, while THG (cyan) enhances the nuclei. The information revealed by each mode can be directly compared, providing a better understanding of the tissue. For example, SHG/THG-merged signals can be used to distinguish the epithelial/stromal interface. It is worth mentioning that these differences and
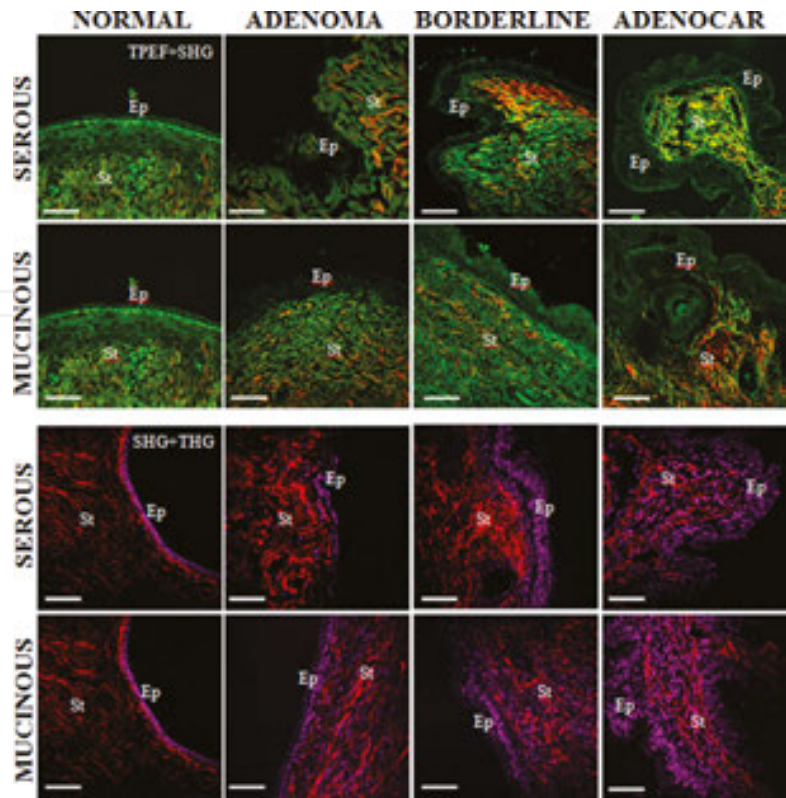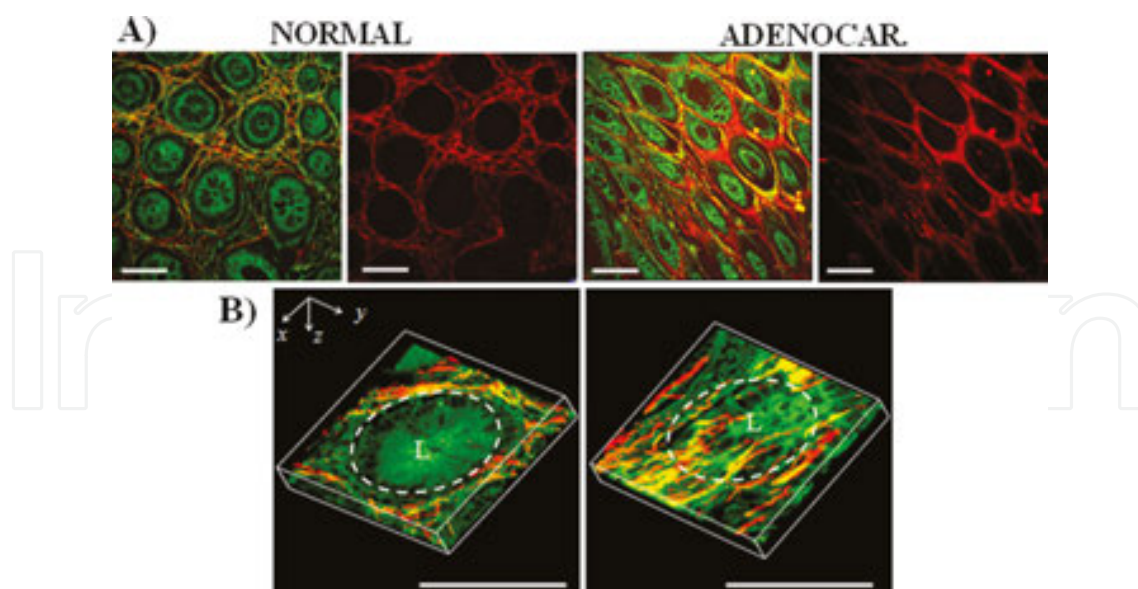
Figure 4. Multimodal NLO approach applied to human ovarian tumor. Representative merges of TPEF (green) and SHG (red) cross-sectional images of ovarian tumor tissues diagnosed as serous-type tumor and mucinous-type tumor; and representative merges of SHG (red) and THG (cyan) cross-sectional images. All scale bar = 20 μm. Ep, epithelium; St, stroma; n, nucleus; c, collagen; Ade, adenoma; Bord, borderline; Adenocar, adenocarcinoma. Reproduced figures from Adur et al. [34] (open access).

contrasts could be automatically and digitally done for quantification (see next section). These data confirm the fact that normal ovaries are more organized tissues than the adenocarcinoma samples. Finally, using THG signal, it was possible to evaluate the differences in the surface epithelium of each tumor type. In normal ovary, cells were arranged in one cell layer. Serous adenoma samples display elevated ciliated and non-ciliated cuboidal epithelial cells with lengthened nuclei, also in one regularly single cell layer. Besides, the serous borderline tumor and serous adenocarcinoma samples are absolutely different from the previous ones, showing epithelial surface with cells of altered sizes lying in multiple layers, including cellular atypia and proliferation. Mucinous tumor samples are similar to borderline/adenocarcinoma, with different size cells forming up multiple layers, but having rich cytoplasmic mucin and basal nuclei.

Figure 5 summarizes the combined uses of these techniques in the analysis of human colon cancer. NLO images clearly demonstrate the circular arrangement pattern of control colonic crypts registered from crypt-cross sections, characterized by epithelial columnar cells and interspersed goblet cells. TPEF (green) revealed the typical foveolar pattern of colon mucosa glands, displaying crypts with rounded luminal openings. SHG (red) specifically traces the collagen scaffold within lamina propria. The evaluation of colonic tissue by SHG microscopies

Figure 5. Multimodal NLO approach applied to human colon tumor. (A) Representative TPEF+SHG and SHG cross-sectional images of normal and tumor colon tissues. Scale bars = 20 μm. (B) Maximum projection of 60 images separated 0.5 μm each of normal and adenorcarcinomas colonic tissues. Epithelial-stromal interface is indicated (white outline). Scale bars = 50 μm. L, luminal crypt orifice; Adenocar, adenocarcinoma. Reproduced figures from Adur et al. [37] (open access).

rapidly and clearly allows differentiating between adenocarcinoma and normal tissue states. Whereas individual crypts were easily identified with TPEF, the interspersed connective tissue was detected via SHG of collagen (**Figure 5A**). As was previously stated, in tumoral tissues, SHG images highlight changes in the surrounding fibrous stroma. Another key aspect of NLO techniques in relation to the classical H&E ones is that they have high potential to produce 3D reconstructions and stereological studies. **Figure 5B** shows three-dimensional representations that allow the visualization of indistinguishable features in classical two-dimensional procedures. Using 3D SHG representation, it was possible to detect the tilt and invasiveness of collagen fibers of adenocarcinomas compared to normal colon. Those features are not easily visible in standard two-dimensional H&E-stained sections. In others works, NLO microscopy approaches, especially when combined, can reveal information not distinguishable in H&E stained sections. Different changes in collagen fibers are parameters that can be consistently quantified, which allows to predict an enormous clinical potential in colon cancer. These results show important changes of collagen fiber morphology, alignment, and density in colon tumor tissue, suggesting that collagen fiber inclination angles are a key factor in tumor progression. In agreement with these results, previous reports on human colon and other tissues suggest that the epithelial cells preferentially invade tissues where the collagen fibers became perpendicularly aligned, instead of arbitrarily organized ones [35, 36].

3.2. Osteogenesis imperfecta

Osteogenesis imperfecta (OI) is a heterogeneous disorder of connective tissues (see **Table 2** for types of OI) with an incidence of 1/15000 [38, 39] and disease severity spanning from subclinical

osteoporosis to intrauterine lethality. Dominant mutation in collagen type I is the most common cause (>90%). Type I collagen is the most abundant extracellular matrix (ECM) protein in humans and the major structural protein in many organs, for example in skin. It is a heterotrimer consisting of two α1-chains and one α2-chain, encoded by COL1A1 and COL1A2, respectively. Mutations in the genes encoding type I procollagen produce a range of disorders, which include autosomal dominant (AD) OI. Currently, more than 1000 heterozygous COL1A1/2 mutations have been identified (https://oi.gene.le.ac.uk) [40, 41]. Mutation type and position influence the phenotype and as such genotype-phenotype relations exist to some extent. Mainly, two types of mutations in collagen I cause classical dominant OI: quantitative and qualitative collagen defects. These collagen I mutations are reflected in some way on fibril collagen assembly that can be finally observed in an organ, such as the skin. For example, in patients suffering from OI, skin collagen fibers could be smaller and more randomly packed. These disorders in collagen fibrils could be quantified using SHG microscopy.

| Type | I | II | III | IV | V | VI |
Characteristic						
Severity	Mild	Perinatal lethal	Severe	Moderate	Moderate	Moderate
Congenital fractures	NO	YES	Usually	Rarely	NO	NO
Bone deformity	Rarely	Very severe	Severe	Mildly moderate	Moderate	Moderate
Stature	Normal	Severely short	Very short	Variable short	Variable	Mildly short
Hearing loss	60% of cases	NA	Common	42% of cases	NO	NO
Respiratory complications	NO	YES	YES	NO	NO	NO

NA: not available

Table 2. Clinical characteristics of osteogenesis imperfecta.

Figure 6 depicts representative images acquired using previous setup, displaying representative TPEF (green) and SHG (red) images. TPEF signals are generated fundamentally by the eosin fluorescence and, in every case, this signal was used to detect just the skin epithelium (dashed white line). The non-contamination confirmation of the SHG signal was established by the wavelength range, half of the excitation, of the signal, by using the avalanche photodiodes (APD) array of the LSM-780 Zeiss scan head CCD. Besides the difference found in the collagen extent, a visual examination of the SHG images of **Figure 6** reveals that the normal skin has thinner collagen fibers that weave in all directions round the hair follicles. The skin from OI patients exhibits changes in collagen fiber thickness when compared to the normal skin. Skin images from the more severe forms of OI result in thicker, broken, and wavy collagen fibers that are firmly packed following the same direction. Moreover, using fresh skin, one can identify a marked reduction in the density of the collagen fibers network in the 3D illustration of SHG images from severe OI patient's samples (**Figure 6B** and **6C**), when compared with 3D SHG images from normal skin fresh biopsies (**Figure 6A**). These skin images are just a basic representative example about how the SHG tool can be used for optical evaluation of OI.
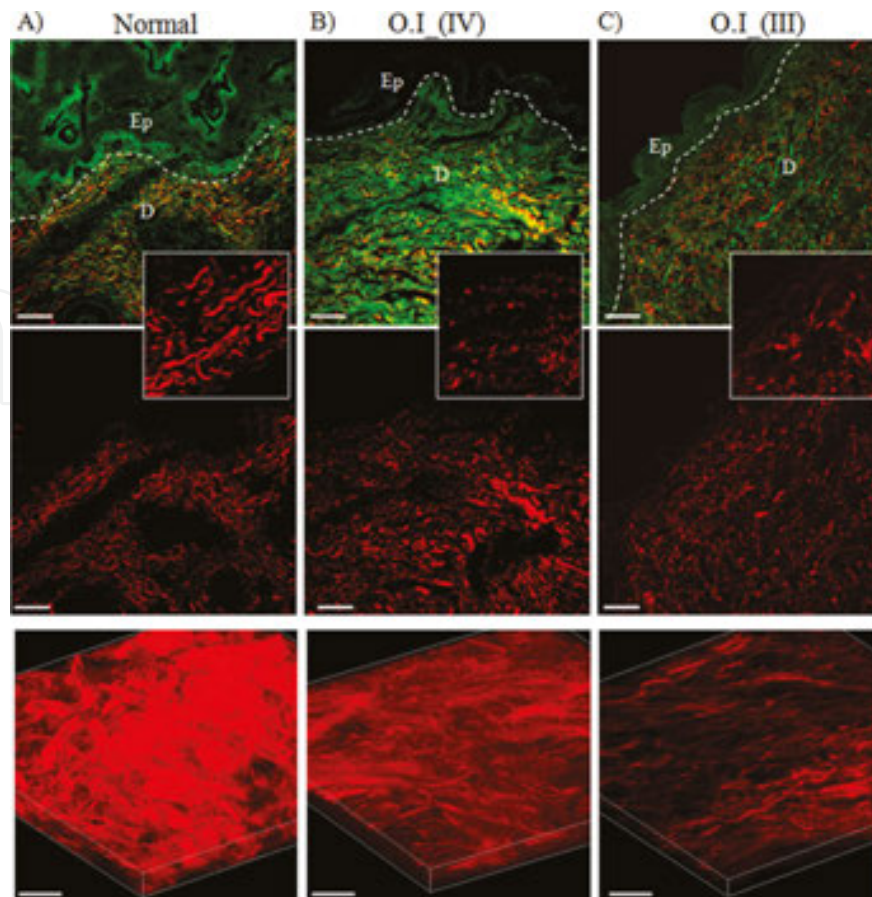
Figure 6. Representative cross-sectional images for TPEF (green) and SHG (red) analyses of normal (A), OI type IV (B), and OI type III (C) skin human tissues. Epidermis/dermis interface is signposted by white outline. Insets highlight visual differences of fiber collagen. Ep, epidermis; D, dermis; and representative 3D maximum projection (40 images at intervals of 1 μm) of SHG images from fresh skin biopsies. Scale bars = 20 μm. Reproduced figures with permission from Journal of Biomedical Optics, 2012 [19].

However, to offer a more accurate diagnostic method, it is necessary to develop reliable quantitative tools that allow discriminating between different OI types. The following section aims to demonstrate that the texture analysis (one of the analyses method presented below), which is the first step to provide SHG image quantitation tool, providing important information about collagen fiber organization.

4. Analysis methods used as diagnostic tools

As was previously mentioned, different processing methods can be used to obtain the relationship between signals of epithelial cells and the collagen matrix obtained with NLO microscopy techniques [4, 42]. Some of the methods that are currently used and others potentially implementable with free software, such as ImageJ (NIH, Bethesda, Maryland, USA), are described below.

### 4.1. Ratio between collagen and elastic tissue (SAAID)

The second harmonic to autofluorescence aging index of dermis (SAAID) value is a measure of the ratio between collagen and elastic fiber network [4, 43]. As the stroma is composed primarily of collagen and elastic fibers allows the use of nonlinear optical signals to discriminate between altered connective tissue regions near tumor area [44–46]. Specifically, collagen fibers are strong second harmonic signal generators, whereas elastic fibers are only autofluorescent emitters. This parameter can be applied when TPEF and SHG microscopy are simultaneously used [47, 48]. The SAAID index is defined as SAAID = $(I_{SGH} - I_{TPEF})/(I_{SHG} + I_{TPEF})$, where I equals the intensity of each signal, SHG/TPEF are above preselected threshold intensities [43]. For example, to obtain this index, we have used the collagen-elastic tissue ratio map in the whole image of ovarian tissue (**Figure 7A, B**). The whole stroma region was selected as one ROI for each image. It has been demonstrated that collagen content was increased within the tumor stroma. The quantification of these observations is showed by the SAAID bar graph (**Figure 7C**). The corresponding SAAID of adenocarcinoma type exhibits statistically significant ($p<0.05$, t-test) higher values (-0.38 ± 0.03) compared to normal stroma (-0.63 ± 0.06) due to the high SHG (collagen) signal and low TPEF signal in this region. To demonstrate the utility of this index, it was applied to images of ovarian cancer showed in **Figure 4** and represented by bar graph in the **Figure 7D**. The corresponding SAAID of both adenocarcinoma types presented statistically significant ($p<0.05$, t-test) higher values compared to normal stroma due to both the high SHG (collagen) and low TPEF signals in this region [34].

4.2. Tumor-associated collagen signatures (TACS)

This parameter is frequently used to determine the collagen fiber orientation at the tumor stroma boundary [4]. At present, there are three well-characterized TACS. They are reproducible during defined stages of tumor progression: TACS-1 (presence of dense collagen localized around small tumors during early disease), TACS-2 (collagen fibers arranged parallel to the tumor boundary—around 0°), and TACS-3 (collagen fibers disposed perpendicularly to the tumor boundary—around 90°, when the disease becomes invasive) [49]. The collagen-fiber angle calculation (relative to the tumor boundary) is required to know the epithelial zone having abnormal appearance. After this manual selection, fiber angle could be measured using the angle tool option from ImageJ toolbar. This tool measures the angle demarcated by three points. The first is an arbitrary point-guide along the fibril; the second one is the fibril extreme, closer to edge of the tumor; and the third one is any point that connects to the first draws with a path parallel to the epithelium [20]. Using this parameter, for example, to analyze collagen transformation in ovarian cancer, the fiber angle relative to the epithelium has been quantified. SHG images have been used along with collagen orientation, instead of the SHG signal (**Figure 7E, F**). The TACS-2, straightened (taut) collagen fibers, stretched around the epithelium (**Figure 7E**), and TACS-3, identifying radially aligned collagen fibers, that may provide the scaffolding of local invasion (**Figure 7F**), has been found. In normal ovary tissue, collagen fibers were mainly distributed around 0° (see white arrows). Approximately 75% of these fibers are parallel to the epithelium (angle ≤ 20°). In contrast, serous adenocarcinoma exhibits incipient

regions of local invasion (TACS-3) with a set of realigned fibers, most of which are disposed around 90° (see white arrows) with respect to epithelium (**Figure 7G**) [4, 20].
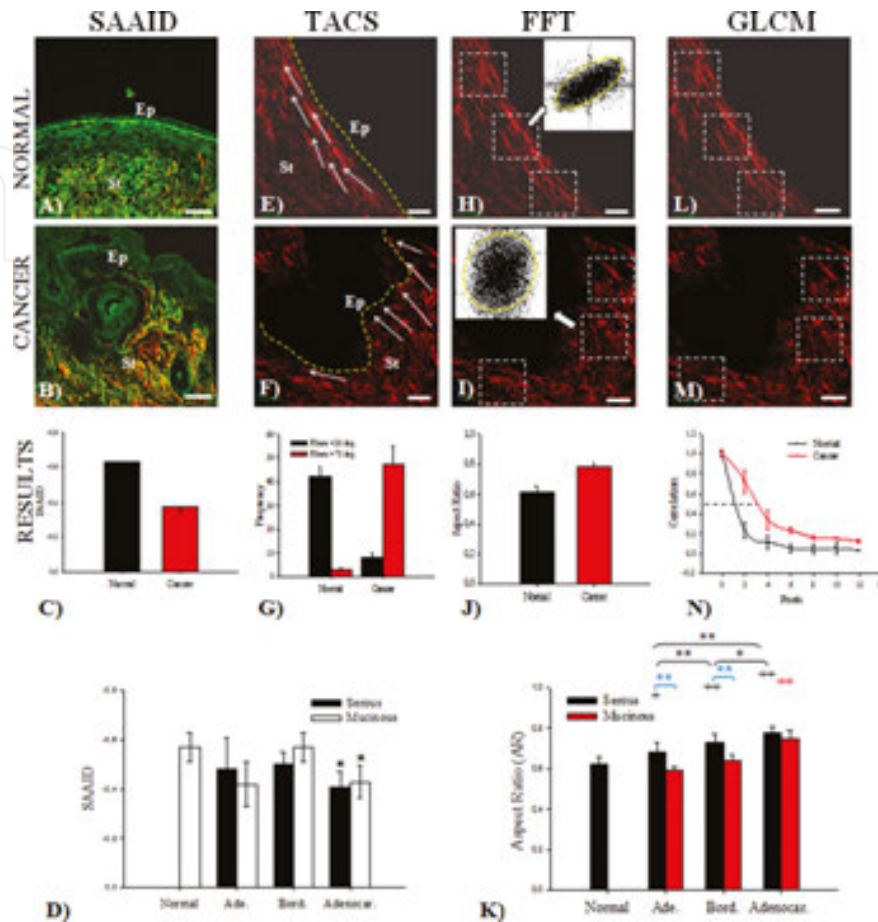
Figure 7. Depicting several applications of different methods to analyze NLO signals. The panel shows representative TPEF (green) and SHG (red) images of (A, E, H, L) normal and (B, F, I, M) cancer ovary. From the TPEF+SHG combination (first column), it is possible to calculate (C) the SAAID ratio. From the SGH image (remaining columns) and using regions near the epithelial/stromal interface (yellow line), it is possible to calculate: (G) TACS (measuring the collagen fiber angle relative to the epithelium); (J) FFT transforms (and fit to ellipse to estimate the anisotropy); and (N) GLCM (correlation value). (D) Bar graphs represent SAAID index quantitative analysis of ovarian tissues. Asterisks indicate a significant increase as compared to the nontumor tissues ($p<0.05$, t-test). (K) Bar graphs represent anisotropy (aspect ratio) quantitative analysis of ovarian tissues. Comparisons with normal tissues are indicated with +. +,* indicates a statistically significant ($p<0.05$) difference and ++, ** indicates a statistically very significant ($p<0.01$) difference following ANOVA. Ep, epithelium; St, stroma; white arrows, collagen fibers; white squares, regions of interest (ROI). Reproduced figures from Adur et al. [4] (open access).

4.3. Fast Fourier transform (FFT) analysis

The FFT has proven to be a good method to assign the degree of image organization [42, 50]. Thereby, the FFT of a set of aligned fibers will have higher values along the orthogonal path to the direction track of the fibers, and its intensity plot seems to have an ellipsoidal shape. If the fibers are perfectly aligned, the ellipse will collapse into a line. For randomly oriented fibers, the intensity plot of the corresponding FFT image looks like a circle. Therefore, the anisotropy

of the image can be calculated by performing an elliptic fit on the thresholded FFT images, and then calculating the ratio between its short and long axes, i.e., its aspect ratio (AR) [51]. One sample will be more anisotropic as the AR goes to zero, whereas it will be more isotropic when the AR is closer to one.

To perform anisotropy calculations, squared ROI in the SHG images are usually selected, with the only requirement that they must be placed upon the collagen network around the epithelium, since this is the region responsible for the stroma invasion. The square ROI is required by the FFT procedure of ImageJ, based on an implementation of the 2D Fast Hartley Transform [52]. The FFT can be carried out with the homonymous command of the ImageJ menu [4]. The anisotropy on the ovary SHG image of stromal region has been estimated using this methodology (**Figure 7H, I**). Three ROIs of 150×150 pixels side squared have been used to ensure that the collagen network in the vicinity of the epithelium is registered. **Figure 7J** shows the AR value averaged on all the examined samples. In serous-type tumors, it was found that the AR index turned out to be significantly increased ($p < 0.05$, t-test) from normal (0.62 ± 0.04) to adenocarcinoma samples (0.78 ± 0.03).

Using this method, serous and mucinous ovarian cancer samples were analyzed (**Figure 4**). In serous-type tumors, AR increased progressively and significantly ($p < 0.05$, ANOVA) from normal to adenocarcinoma, and in mucinous-type tumors (by contrast), AR showed statistically very significant differences only for adenocarcinomas ($p < 0.01$, ANOVA) (**Figure 7K**). These results confirm the fact that normal ovaries are more organized tissues as compared to adenocarcinoma. By using this tool, it was possible to discriminate between serous adenoma from mucinous adenoma and serous borderline from mucinous borderline subtypes [48]. Unlike ovarian serous tumors, which are relatively homogeneous in their cellular composition and differentiation degree, mucinous tumors are frequently heterogeneous, with mixtures of benign, borderline, and malignant elements often found within the same neoplasm. The heterogeneity in these mucinous tumors suggests that malignant transformation is sequential and slow, progressing from cystoadenoma to borderline tumor and, finally, to invasive carcinoma [46]. This slow behavior is probably reflected in a more organized stroma [53].

4.4. Gray level co-occurrence matrix (GLCM) analysis

The GLCM analysis method allows the classification of different tissues based on the evaluation of geometrical collagen arrangement [4, 42]. It provides information on the spatial relationships between pixel brightness values in a given image. The GLCM is constructed by counting the number of occurrences of a gray level adjacent to another gray level, at a specified pixel distance "d" and dividing each counting by the total counting number to obtain a probability. The result is a matrix with rows and columns representing gray levels and elements containing the probability $P_d[i,j]$ of the gray-level co-occurrence between pixels. The matrix is usually averaged in opposite and different orientations (0–180°, 45–225°, 90–270°, and 135–315°) unless one-dimensional feature dominates overall possible ones, in which case, the 0–180 average is sufficient. A detailed explanation on how this matrix is created from the original image can be found in [54].

The GLCM analysis can be carried out by different methods; they are commonly classified as contrast methods, orderliness methods, and statistical methods. Contrast methods can be used in order to give quantitative information on the intensity fluctuations in the image [4, 34, 42]. Among the contrast methods, homogeneity is the weighted sum of the GLCM pixel values. The weights are values nonlinearly decreasing according to the distance from the GLCM matrix diagonal increases. The homogeneity parameter gives information about the similitude of two neighboring pixel values, against all the other pair of pixels of the image. Orderliness methods are particularly suitable to images with fibrous structures, such as SHG images of collagen. This approach can be used in order to give a quantitative measurement on the mutual orientation of collagen fiber bundles. The energy parameter, for example, is the root-squared sum of the GLCM pixel values. Considering that it gives higher weight to the hot spots of the GLCM matrix, that parameter can be considered as a measure of the sample orderliness. Statistical methods are based on the statistical analysis of pixel value dependence and can be used for determining repetition of a certain pattern within a tissular image. Among them, the correlation method probably represents the most powerful approach to be applied to SHG images of collagen. Mathematically the parameters are defined in **Table 3**.

| Parameters	Interpretation	Mathematical expression
Correlation	Linear dependency of gray levels on those of neighboring pixels	$-\sum_{i,j=0}^{N-1} P_{i,j}\left[\frac{(i-\mu)(j-\mu)}{\sigma^2}\right]$
Contrast	Representation of pixels entirely similar to their neighbor	$\sum_{i,j=0}^{N-1}(i-j)^2 P_{i,j}$
Energy	Degree of image's texture directions according to the perception of human eyes	$\sum_{i,j=0}^{N-1} P_{i,j}^2$
Homogeneity	Measure of the amount of local uniformity present in the image	$\sum_{i,j=0}^{N-1}\frac{P_{i,j}^2}{1+(i-j)^2}$

Table 3. GLCM parameters and its mathematical expressions.

The texture analyses can be performed with Image-J GLCM Texture plugin, which was described by Walker and collaborators [55]. Also other parameters such Contrast, Entropy, Inertia, and Variance could be estimated from the GLCM approach [42]. Here a characterization of tissues by estimating the typical dimensions in which collagen maintains its organization is showed. For example, the correlation of the image itself with a pixel separation translated from 1 to 12 or 18 pixels (**Figure 7L–N**) was used. The feature was averaged at angles θ = 0, 90, 180, and 270 degrees to take into account the fact that these images do not have a specific spatial orientation. The distance where correlation falls to 1/2 expressed in microns was measured [4]. To perform the calculations, three ROIs (100×100 pixel side squared) in the SHG images near the epithelium were selected. Correlation and entropy were measured using GLCM-Texture plugin from ImageJ, which was previously described by Walker and collaborators [55]. **Figure 7N** shows that the correlation of normal fibrils fall off sharply with distance,

indicating distinct, linear fibrils, whereas correlation for the fibrils in adenocarcinomas remained elevated for larger distances, implying less-defined fibrillar structure. Consistent with qualitative appearances, the correlation was found to remain higher in malignant tissues with the Corr50, the pixel distance where the correlation dropped below 50% of the initial value, significantly greater in adenocarcinomas (3.4 pixels) compared with normal ovarian (1.7 pixels) (**Figure 7N**; $p<0.05$, t-test). In the same ROI, the entropy values were 6.26 ± 0.31 and 7.40 ± 0.58 from normal and adenocarcinoma, respectively. This means that normal tissues exhibit a lesser complexity or higher organization than malignant ones [34].

Following the impact of GLCM analysis, the method in the evaluation of patients with OI is showed. Skin samples from healthy and from patients with OI were obtained from the Laboratory of Pediatric Endocrinology, Campinas, SP, Brazil. Biopsies were analyzed and classified as normal (4 cases) or OI (5 cases). OI patients were classified according to clinical observations in mild OI (Type I—1 case), moderately affected and severe OI (Type III or Type IV—4 cases). Normal samples were obtained from eyelid plastic surgery discarded tissue, and patient biopsies were obtained from growing skin. Fresh skin samples in Phosphate Buffer Solution (PBS) were analyzed by 3D SHG representations within 6 hours of the excision. From the mounted SHG pictures, images located in the dermis were taken. Nonsymmetric GLCMs were computed using 256 gray levels. Because collagen fiber orientation changed from sample to sample, four orientations average were used. This scoring method was competent to satisfactorily discriminate the different OI patients according to their clinical severity [56]. Using fresh biopsies, one could detect a marked density decrease of the collagen fibers network in the 3D representations of SHG images from severe OI patient's samples (**Figure 8B** (Type III) and **Figure 8C** (Type IV)), when compared with the 3D representation of SHG images taken from normal skin fresh biopsies (**Figure 8A**). Furthermore, energy value of GLCM texture analysis could not only discriminate type I and type III OI samples from normal skin (**Figure 8D**), but it could also differentiate (with statistical significance) between patients with varying degrees of OI, including Type IV OI (**Figure 8E**). It is well known that dermis collagen fibers have diameter ranges around 0.5 to 3 μm. Therefore, it is expected that GLCM analysis would show a repeating structure with distances of about 1.5–8 pixels corresponding to the 0.5–3 μm range. Considering that OI patients exhibit thicker fibers than normal skin samples, GLCM correlation signals could be to drop on a longer scale. The values of decay length are obtained by fitting the correlation data with a double exponential decay function. The decay length values using the Corr50 (the pixel distance where the correlation dropped below 50% of the initial value) obtained are between 1.3 and 2.5 μm (3.8–7 pixels), confirming that patient D had thicker collagen fiber ≈ 2.5 μm (7 pixels). Using this pixel distance as comparison, the energy parameter shows values of 0.15 ± 0.02 (normal), 0.13 ± 0.04 (Patient (Pat.) A), 0.20 ± 0.03 (Pat. B), 0.24 ± 0.04 (Pat. C), 0.29 ± 0.03 (Pat. D), and 0.33 ± 0.04 (Pat. E), with significant differences ($p<0.05$) when normal skin was compared with OI patient's (B, C, D, and E) skin. This means that this texture parameter clearly allows the identification of each patient pattern. Interestingly, by using this method, it was possible to discriminate one case of type IV patient, exhibiting a more severe phenotype (Patient D) than the others. SHG images of these patient skins display a more compacted collagen pattern (thicker collagen fiber), intermediate between type III, and the two remaining type IV patients. The preliminary results allow auguring that

these nonlinear microscopy techniques in association with specific scoring method (energy-GLCM) will be an excellent diagnostic tool to clinically distinguish different types of OI in human skin [56].
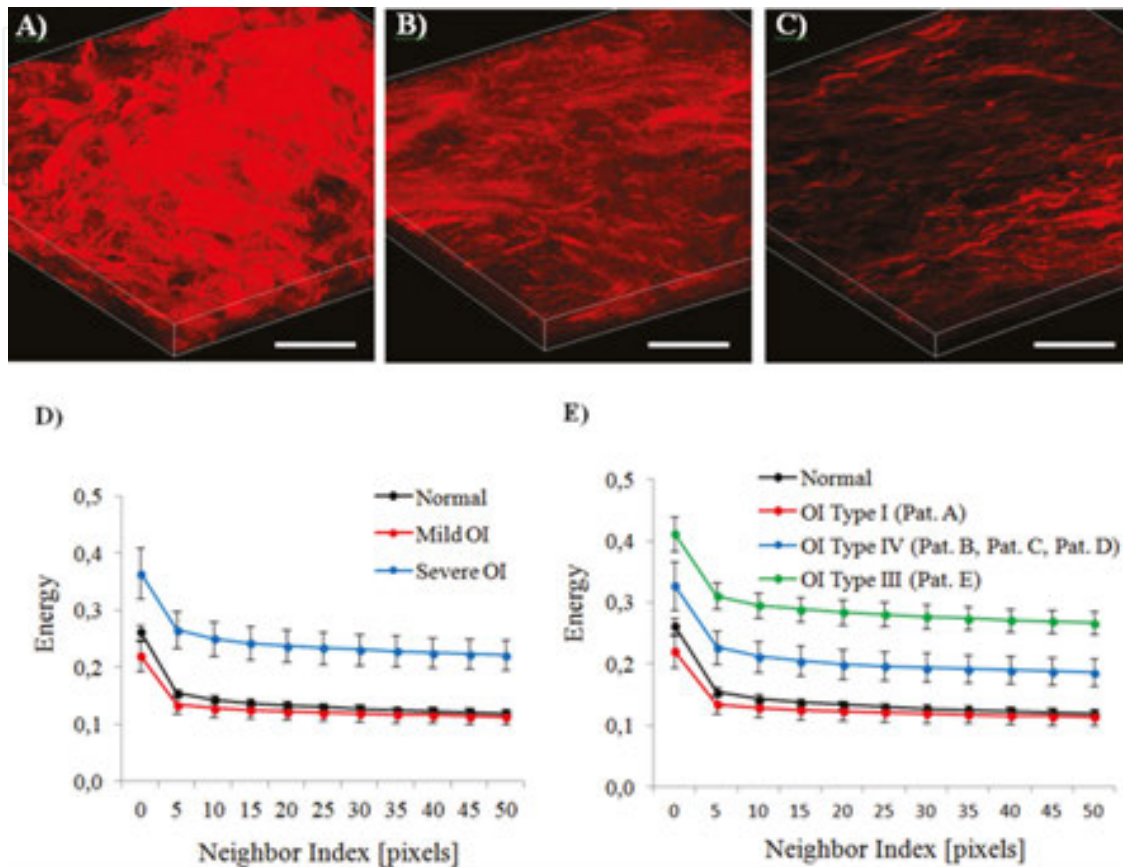
Figure 8. Representative 3D maximum projection (40 images at 1μm interval) of SHG images from fresh skin biopsies, (A) normal skin, (B) OI type III (Patient E), and (C) OI type IV (Patient D). Texture analysis (D, E) using GLCM. Energy values were calculated in dermis tissues versus distance pixels; ranging from 1 to 50 pixels (0.35 μm–17.30 μm) in 0, 45, 90, and 135° directions of image (d): $n = 12$ normal, $n = 3$ mild OI, and $n = 12$ severe OI; and (e) $n = 12$ normal, $n = 3$ OI type I, $n = 9$ OI type IV, $n = 3$ OI type III). Pat: patients. Reproduced figures from Adur et al. [56] (open access).

5. Conclusions

This chapter summarizes several nonlinear microscopy techniques that can be combined and the images acquired analyzed by a set of quantitative tools. This may allow the implementation of new diagnostic procedures for early detection of various diseases. The integration of a set of microscopy techniques is one of the evolving areas in bioimaging that promises to have a strong impact on the understanding and early detection of diverse pathologies. As has been described and exemplified in the sections of this chapter, the advantages of the techniques are numerous, namely high depth penetration (due to Near Infrared (NIR) laser), intrinsic 3D

sectioning and 3D resolution (due to the spatial confinement of the signal to the laser focus), multiple nonlinear processes summed to the possibility to detect several endogenous molecular markers, and low phototoxicity. Additionally, these techniques allow the investigation of living processes in the native environment without major perturbations. All these advantages allow us to postulate that in the near future the NLO techniques together with nonlinear signal processing methods can be very useful in the field of medical diagnosis. In combination with sophisticated animal models and computer-assisted data analysis, NLO microscopy techniques and image processing methods are opening new doors to the study of tumor biology, facilitating the development of new strategies for early tumor diagnosis and other diseases.

As is shown in this chapter, by integrating the strengths of each NLO imaging modality, different structures, and their interactions in a complex biological system can be simultaneously visualized. Additionally, the possibility of obtaining images at high speed and with chemical specificity makes NLO microscopy a powerful tool to evaluate the dynamic behavior of *in vivo* disease progression [57]. CARS microscopy should allow longitudinal studies of lipid metabolism in the same living model organisms over time. Other auspicious application is the label-free imaging of organogenesis and drug delivery. Also, CARS can provide structural information and it has been useful in analyzing molecular orientations in myelin [58], single lipid bilayer [59], cellulose fiber [60], and crystal of clean fourth-order symmetry [61].

In translational research, NLO microscopy has demonstrated the ability of diagnosing diseases of live organisms [62]. Recently, it has been found that changes occurring in collagen deposit and arrangement, in early tumor development and during their progression, can be used as predictable tools of the disease status. The ovary examples in this work demonstrate that AR and correlation analysis have the ability to predict the disease degree in human patients. Therefore, if more experiments are successful, SHG may eventually provide a more rapid, real-time substitute for traditional histopathological processing and analyses. For this disease, mortality rates are elevated because an efficient screening test does not exist presently. Approximately, 15% of ovarian cancers are found before metastasis has occurred. If ovarian cancer is found and treated before this process is triggered, the 5-year survival rate will be around 94%. Thus, an early diagnostic test to detect premalignant changes would save many lives. In this sense, the unique attributes of NLO microscopy described here render these methods as a promising imaging modality for disease diagnostics in the clinic. Also, the medical utility of these optical methods could be improved by the continuous development and refinement of methods to obtain objective, quantitative information. These will be in the form of analysis algorithms such as Helmholtz analysis, wavelet analysis, and with numerical parameters relating to image frequency content and second-order gray-level statistics. Further, a classification scheme could be developed by using a support vector machine.

The effort to develop new diagnosing methods that could better identify early lesions and consequently lead to an early diagnosis is a challenge and a stimulus for research in this area. The outcomes of different works indicate that the combination of diverse image analysis approaches summarized here represent a combination of powerful tools to investigate epithelial cells transformation, collagen organization, and extracellular matrix remodeling in epithelial tumors and *osteogenesis imperfecta* in skin. About OI, it was demonstrated in this

chapter that nonlinear microscopy techniques, in combination with image analysis approaches, represent a powerful tool to investigate the collagen organization in skin dermis in patients with OI and having the potentiality to distinguish the different types of OI. The procedure used here requires a skin biopsy, which is almost painless as compared to the bone biopsy commonly used in conventional methods. The data presented here are complementary of existing clinical diagnostic approaches and can be used as a procedure to confirm the disease and evaluate its severity and treatment efficacy.

In cancer diagnosis, there is a growing need for the development of a multimodal imaging-based diagnostic tool to objectively evaluate morphological features with subcellular resolution and molecular compositions that are closely associated with tumor malignancy. With this perspective, NLO microscopy has proven to be useful in cancer research. These techniques have recently emerged as a valuable tool for high-resolution, nondestructive, chronic imaging of living tumors. Moreover, multimodal microscopy can provide a powerful tool for investigating the dynamics of structure-function relationships both at the subcellular and molecular levels.

Today, the application of multimodal nonlinear imaging is recognized in basic research in the biological and biomedical sciences; however, regular applications in clinics are still rare, mainly because of their high cost. Multimodal platforms are still complex and require specialized personnel for its operation. So, mainly technological progresses are required for miniaturization, enhancement of the ease of control, automated data processing, and extraction of significant information. To achieve this goal, the modification of typical clinical endoscopes for in vivo multimodal nonlinear imaging is necessary. The development of nonlinear optical endoscopy, which allows imaging under conditions in which a conventional nonlinear optical microscope cannot be used, will be the primary goal to extend applications of nonlinear optical microscopy toward clinical ones. There are several key challenges involved in the pursuit of in vivo nonlinear optical endoscopy. A few of them are the necessity of obtaining efficient ultrashort pulse laser liberations into a remote place, the need to enhance scan rates for monitoring biological processes, and the miniaturization of the laser-scanning mechanisms to the millimeter scale. Finally, the design of a nonlinear optical endoscope based on micro-optics with great flexibility, and compact enough to be incorporated into endoscopes, will become an evolution of these microscopy platforms. With the continuous advancement in this endoscopic techniques and new laser sources, we have reason to believe that these particularly promising techniques in conjunction with efficient image analysis algorithm will open up many new possibilities for the diagnosis and treatment of different diseases in the near future.

Acknowledgements

Author details

Javier Adur[1,2,3*], Hernandes F. Carvalho[3,4], Carlos L. Cesar[3,5,6] and Víctor H. Casco[1,2]

*Address all correspondence to: jadur@bioingenieria.edu.ar

1 CITER—Centro de Investigación y Transferencia de Entre Ríos, UNER-CONICET, FI-UNER, Argentina

2 Microscopy Laboratory Applied to Molecular and Cellular Studies, School of Bioengineering, National University of Entre Ríos, Argentina

3 INFABiC—National Institute of Science and Technology on Photonics Applied to Cell Biology, Campinas, Brazil

4 Department of Structural and Functional Biology, Biology Institute, State University of Campinas, Brazil

5 Biophotonic Group, Optics and Photonics Research Center (CEPOF), Institute of Physics "Gleb Wataghin", State University of Campinas, Brazil

6 Department of Physics of Federal University of Ceara (UFC), Brazil

References

[1] Provenzano PP, Eliceiri KW, Keely PJ. Multiphoton microscopy and fluorescence lifetime imaging microscopy (FLIM) to monitor metastasis and the tumor microenvironment. Clin. Exp. Metastasis. 2009; 26:357–370. doi: 10.1007/s10585-008-9204-0

[2] Masters BR, So PTC. The genesis of nonlinear microscopies and their impact on modern developments. In: Master and So, Editors. Handbook of Biomedical Nonlinear Optical Microscopy. New York: Oxford University Press, 2008. p. 5–28.

[3] Meyer T, Schmitt M, Dietzek B, Popp J. Accumulating advantages, reducing limitations: multimodal nonlinear imaging in biomedical sciences – the synergy of multiple contrast mechanisms. J. Biophotonics. 2013; 6:887–904. doi: 10.1002/jbio.201300176

[4] Adur J, Carvalho HF, Cesar CL, Casco VH. Nonlinear optical microscopy signal processing strategies in cancer. Cancer Inf. 2014; 13:67–76. doi: 10.4137/CIN.S12419

[5] Shen YR. The principles of nonlineal optics. New York, John Wiley, 1984.

[6] Gu M, Bird D, Day D, Fu L, Morrish D. eds. Nonlinear optical microscopy. In: Femtosecond Biophotonics Core Technology and Applications. New York: Cambridge University Press, 2010. p. 9–34.

[7]   Cheng PC, Sun CK. Nonlinear (harmonic generation) optical microscopy. In: Pawley JB, Editor. Handbook of Biological Confocal Microscopy, 3rd edn. 2006. Springer. New York. p. 703–721.

[8]   Gauderon R, Lukins PB, Sheppard CJ. Three-dimensional second-harmonic generation imaging with femtosecond laser pulses. Opt. Lett. 1998; 23:1209–1211.

[9]   Chu SW, Chen IH, Liu TM, Chen PC, Sun CK, Lin BL. Multimodal nonlinear spectral microscopy based on a femtosecond Cr:forsterite laser. Opt. Lett. 2001; 26:1909–1911.

[10] Boyd R. Nonlinear Optics, 1st edn. New York, Academic Press, 1992.

[11] Debarre D, Beaurepaire E. Quantitative characterization of biological liquids for third harmonic generation microscopy. Biophys. J. 2007; 92:603–612.

[12] Williams RM, Zipfel WR, Webb WW. Interpreting second-harmonic generation images of collagen I fibrils. Biophys. J. 2005; 88:1377–1386.

[13] Campagnola PJ, Millard AC, Terasaki M, Hoppe PE, Malone CJ, Mohler WA. Three-dimensional high-resolution second-harmonic generation imaging of endogenous structural proteins in biological tissues. Biophys. J. 2002; 82:493–508.

[14] Chu SW, Chen SY, Chern GW, Tsai TH, Chen YC, Lin BL, Sun CK. Studies of chi(2)/chi(3) tensors in submicron-scaled bio-tissues by polarization harmonics optical microscopy. Biophys. J. 2004; 86:3914–3922.

[15] Müller M, Squier J, Wilson KR, Brakenhoff GJ. 3D microscopy of transparent objects using third-harmonic generation. J. Microsc. 1998; 3:266–274.

[16] Moreaux L, Sandre O, Blanchard-Desce M, Mertz J. Membrane imaging by simultaneous second-harmonic generation and two-photon microscopy. Opt. Lett. 2000; 25:320–322.

[17] Sun CK, Chu SW, Chen SY, Tsai TH, Liu TM, Lin CY, Tsai HJ. Higher harmonic generation microscopy for developmental biology. J. Struct. Biol. 2004; 147:19–30.

[18] Adur J, Pelegati VB, Costa LF, Pietro L, de Thomaz AA, Almeida DB, Bottcher-Luiz F, Andrade LA, Cesar CL. Recognition of serous ovarian tumors in human samples by multimodal nonlinear optical microscopy. J. Biomed. Opt. 2011; 16:096017. doi: 10.1117/1.3626575

[19] Adur J, Pelegati VB, de Thomaz AA, D'Souza-Li L, Assunção Mdo C, Bottcher-Luiz F, Andrade LA, Cesar CL. Quantitative changes in human epithelial cancers and osteogenesis imperfecta disease detected using nonlinear multicontrast microscopy. J. Biomed. Opt. 2012; 17:081407-1. doi: 10.1117/1.JBO.17.8.081407

[20] Adur J, Pelegati VB, de Thomaz AA, Baratti MO, Andrade LA, Carvalho HF, Bottcher-Luiz F, Cesar CL. Second harmonic generation microscopy as a powerful diagnostic imaging modality for human ovarian cancer. J. Biophotonics. 2014; 7:37–48. doi: 10.1002/jbio.201200108

[21] Duncan MD, Reintjes J, Manuccia TJ. Scanning coherent anti-Stokes Raman microscope. Opt. Lett. 1982; 7:350–352.

[22] Pelegati VB, Adur J, De Thomaz AA, Almeida DB, Baratti MO, Andrade LA, Bottcher-Luiz F, Cesar CL. Harmonic optical microscopy and fluorescence lifetime imaging platform for multimodal imaging. Microsc. Res. Tech. 2012; 75. doi: 10.1002

[23] Hu W, Zhao G, Wang C, Zhang J, Fu L. Nonlinear optical microscopy for histology of fresh normal and cancerous pancreatic tissues. PLoS One. 2012; 7:e37962. doi: 10.1371

[24] Hompland T, Erikson A, Lindgren M, Lindmo T, de Lange Davies C. Second-harmonic generation in collagen as a potential cancer diagnostic parameter. J. Biomed. Opt. 2008; 13. doi: 10.1117. 054050, doi: 10.1117/1.2983664

[25] Sivaguru M, Durgam S, Ambekar R, Luedtke D, Fried G, Stewart A, Toussaint KC Jr. Quantitative analysis of collagen fiber organization in injured tendons using Fourier transform-second harmonic generation imaging. Opt. Express. 2010; 18:24983–93. doi: 10.1364/OE.18.024983

[26] Mouras R, Rischitor G, Downes A, Salter D, Elfick A. Nonlinear optical microscopy for drug delivery monitoring and cancer tissue imaging. J. Raman Spectrosc. 2010; 41:848–852.

[27] Bianchini P, Diaspro A. Three-dimensional (3D) backward and forward second harmonic generation (SHG) microscopy of biological tissues. J. Biophotonics. 2008; 1:443–450. doi: 10.1002/jbio.200810060

[28] Adur J, Carvalho HF, Cesar CL, Casco VH. Nonlinear imaging microscopy: Methodological setup and applications for epithelial cancers diagnosis. In: Fred Wilkins Ed, Nova Science Publishers. Nonlinear optics: fundamentals, applications and technological advances. New York, Nova Publishers, 2014. p. 97–136.

[29] Cheng JX, Xie XS. Coherent anti-Stokes Raman scattering microscopy: instrumentation, theory, and applications. J. Phys. Chem. B. 2004; 108:827–840.

[30] Volkmer A, Book LD, Xie XS. Time-resolved coherent antiStokes Raman scattering microscopy: imaging based on Raman free induction decay. Appl. Phys. Lett. 2002; 80: 1505–1507.

[31] American Cancer Society. Cancer Facts & Figures 2009. Atlanta, American Cancer Society, 2009.

[32] Tsuboi M, Ueda T, Ushizawa K, Ezaki Y, Overman SA, Thomas GJ. Raman tensors for the tryptophan side chain in proteins determined by polarized Raman microspectroscopy of oriented N-acetyl-L-tryptophan crystals. J. Mol. Struct. 1996; 379:43–50.

[33] Tearney GJ, Brezinski ME, Bouma BE, Boppart SA, Pitris C, Southern JF, Fujimoto JG. In vivo endoscopic optical biopsy with optical coherence tomography. Science. 1997; 276:2037–2039.

[34] Adur J, Pelegati VB, de Thomaz AA, Baratti MO, Almeida DB, Andrade LA, Bottcher-Luiz F, Carvalho HF, Cesar CL. Optical biomarkers of serous and mucinous human ovarian tumor assessed with nonlinear optics microscopies. PLoS One. 2012; 7:e47007. doi:10.1371/journal.pone.0047007

[35] Zhuo S, Zhu X, Wu G, Chen J, Xie S. Quantitative biomarkers of colonic dysplasia based on intrinsic second-harmonic generation signal. J. Biomed. Opt. 2011; 16:120501.

[36] Birk JW, Tadros M, Moezardalan K, Nadyarnykh O, Forouhar F, Anderson J, Campagnola P. Second harmonic generation imaging distinguishes both high-grade dysplasia and cancer from normal colonic mucosa. Dig. Dis. Sci. 2014; 59:1529–1534. doi: 10.1007/s10620-014-3121-7

[37] Adur J, Bianchi M, Pelegati VB, Viale S, Izaguirre MF, Carvalho HF, Cesar CL, Casco VH. Colon adenocarcinoma diagnosis in human samples by multicontrast nonlinear optical microscopy of hematoxylin and eosin stained histological sections. J. Cancer Ther. 2014; 5:1259–1269. http://dx.doi.org/10.4236/jct.2014.513127

[38] Kuurila K, Kaitila I, Johansson R, Grenman R. Hearing loss in Finnish adults with osteogenesis imperfecta: a nationwide survey. Ann. Otol. Rhinol. Laryngol. 2002; 111:939–1946.

[39] Stoll C, Dott B, Roth MP, Alembik Y. Birth prevalence rates of skeletal dysplasias. Clin. Genet. 1989; 35:88–92.

[40] Dalgleish R. The human type I collagen mutation database. Nucleic Acids Res. 1997; 25:181–187.

[41] Dalgleish R. The human collagen mutation database 1998. Nucleic Acids Res. 1998; 26:253–255.

[42] Tilbury K, Campagnola PJ. Applications of second-harmonic generation imaging microscopy in ovarian and breast cancer. Perspect. Med. Chem. 2015; 7:21–32. doi: 10.4137/PMC.S13214

[43] Cicchi R, Sacconi L, Pavone F. Nonlinear imaging of tissues. In: Tuchin VV, Editor. Handbook of photonics for biomedical science. New York, CRC Press, 2010. p. 509–545.

[44] Cicchi R, Massi D, Sestini S, Carli P, De Giorgi V, Lotti T, Pavone FS. Multidimensional non-linear laser imaging of basal cell carcinoma. Opt. Express. 2007; 15:10135–10148.

[45] Cicchi R, Sestini S, De Giorgi V, Massi D, Lotti T, Pavone FS. Nonlinear laser imaging of skin lesions. J. Biophotonics. 2008; 1:62–73. doi: 10.1002/jbio.200710003

[46] Lin SJ, Jee SH, Kuo CJ, Wu RJ, Lin WC, Chen JS, Liao YH, Hsu CJ, Tsai TF, Chen YF, Dong CY. Discrimination of basal cell carcinoma from normal dermal stroma by quantitative multiphoton imaging. Opt. Lett. 2006; 31:2756–2758.

[47] Koehler MJ, König K, Elsner P, Bückle R, Kaatz M. In vivo assessment of human skin aging by multiphoton laser scanning tomography. Opt. Lett. 2006; 31:2879–2881.

[48] Lin SJ, Wu R Jr, Tan HY, Lo W, Lin WC, Young TH, Hsu CJ, Chen JS, Jee SH, Dong CY. Evaluating cutaneous photoaging by use of multiphoton fluorescence and second-harmonic generation microscopy. Opt. Lett. 2005; 30:2275–2277.

[49] Provenzano PP, Inman DR, Eliceiri KW, Knittel JG, Yan L, Rueden CT, White JG, Keely PJ. Collagen density promotes mammary tumor initiation and progression. BMC Med. 2008; 6:11. doi: 10.1186/1741-7015-6-11

[50] Sivaguru M, Durgam S, Ambekar R, Luedtke D, Fried G, Stewart A, Toussaint KC Jr. Quantitative analysis of collagen fiber organization in injured tendons using Fourier transform-second harmonic generation imaging. Opt Express. 2010; 18:24983–24993. doi: 10.1364/OE.18.024983

[51] Matteini P, Ratto F, Rossi F, Cicchi R, Stringari C, Kapsokalyvas D, Pavone FS, Pini R. Photothermally-induced disordered patterns of corneal collagen revealed by SHG imaging. Opt Express. 2009; 17:4868–4878.

[52] Arlo RA. Thesis for the degree of Master of Science by Thayer School of Engineering [master's thesis]. New Hampshire, Dartmouth College Hanover, 1990.

[53] Zhuo S, Zhu X, Wu G, Chen J, Xie S. Label-free monitoring of colonic cancer progression using multiphoton microscopy. Biomed. Opt. Express. 2011; 2:615–619. doi: 10.1117/1.3659715

[54] English RS, Shenefelt PD. Keloids and hypertrophic scars. Dermatol Surg. 1999; 25:631–638.

[55] Walker RF, Jackway PT, Longstaff ID. Genetic algorithm optimisation of adaptive multi-scale in GLCM features. Int. J. Pattern Recogn. 2003; 17:17–39.

[56] Adur J, DSouza-Li L, Pedroni MV, Steiner CE, Pelegati VB, de Thomaz AA, Carvalho HF, Cesar CL. The severity of Osteogenesis imperfecta and type I collagen pattern in human skin as determined by nonlinear microscopy: proof of principle of a diagnostic method. PLoS One. 2013; 8:e69186. doi: 10.1371/journal.pone

[57] Huff TB, Cheng JX. In vivo coherent anti-Stokes Raman scattering imaging of sciatic nerve tissue. J. Microsc. 2007; 225:175–182.

[58] Kennedy AP, Sutcliffe J, Cheng JX. Molecular composition and orientation of myelin figures characterized by coherent anti-Stokes Raman scattering microscopy. Langmuir. 2005; 21:6478–6486.

[59] Potma EO, Xie XS. Detection of single lipid bilayers with coherent anti-Stokes Raman scattering (CARS) microscopy. J. Raman Spectrosc. 2003; 34:642–650.

[60] Zimmerley M, Younger R, Valenton T, Oertel DC, Ward JL, Potma EO. Molecular orientation in dry and hydrated cellulose fibers: a coherent anti-Stokes Raman scattering microscopy study. J. Phys. Chem. B. 2010; 114:10200–10208. doi: 10.1021/jp103216j

[61] Munhoz F, Rigneault H, Brasselet S. High order symmetry structural properties of vibrational resonances using multiple-field polarization coherent anti-Stokes Raman spectroscopy microscopy. Phys. Rev. Lett. 2010; 105:123903.

[62] Wang HW, Langohr IM, Sturek M, Cheng JX. Imaging and quantitative analysis of atherosclerotic lesions by CARS-based multimodal nonlinear optical microscopy. Arterioscler. Thromb. Vasc. Biol. 2009; 29:1342–1348. doi:10.1161/ATVBAHA. 109.189316